Motion of unstable two interfaces in a three-layer fluid with a non-zero uniform current

Chihiro Matsuoka

Motion of unstable two interfaces in a three-layer fluid with a non-zero uniform current

Chihiro Matsuoka[1,2,3]‡

[1]Laboratory of Applied Mathemetics, Graduate School of Engineering, Osaka City University, Sugimoto, Sumiyoshi, Osaka 558-8585, Japan
[2]Nambu Yoichiro Institute of Theoretical and Experimental Physics (NITEP), Osaka City University
[3]Osaka City University Advanced Mathematical Institute (OCAMI), Osaka City University

Abstract. The nonlinear motion of two interfaces in a three-layer fluid with density stratification is investigated theoretically and numerically. We consider the situation such that a uniform current is present in one of the three layers. The linear dispersion relation is calculated by the Newton's method, from which the initial conditions for numerical computations are determined. When the uniform current is present in the upper (lower) layer, strong vorticity is induced on the upper (lower) interface, and it rolls up involving the other interface at the late stage of computations. When the current is present in the middle layer, a varicose wave appears at the initial stage, and it evolves into an asymmetric heart-shaped vortex sheet at the last computed stage. These phenomena are presented using the vortex sheet model (VSM) with and without regularizations.

Keywords: Muli-layer interfacial dynamics, Varicose instability, Vortical structure, Density stratification

‡ Corresponding author: cmatsuoka@osaka-cu.ac.jp

1. Introduction

Interfacial dynamics in a layered fluid with density stratification is important in various areas such as geophysical fluid dynamics [21, 60], internal gravity waves [19, 61], and plasma physics [63, 35]. In geophysical fluid dynamics and internal gravity waves, the continuous density profile of an ocean or atmosphere is often approximated to planar multi-component fluid layers of constant densities. A huge number of researches exist for the interfacial dynamics in a two-layer fluid with a single interface; however, few studies exist for the interfacial motion in more than a two-layer fluid, especially for the nonlinear interfacial motion in a three-layer fluid flow. In the current study, we investigate the nonlinear motion of two interfaces in a three-layer fluid with uniform current under gravity, in which the lightest fluid is assumed to lie on the top of the layer, and the heaviest fluid is set at the bottom layer.

The linear analysis for the multi-layer fluid systems have been investigated in detail by Mikaelian [43, 44, 45, 46], in which he derived the eigenvalues and eigenfunctions in the multi-component density stratified Rayleigh-Taylor instability (RTI) [43, 44] and the Richtmyer-Meshkov instability (RMI) [52, 42, 46]. These are typical interfacial instabilities that occur in plasma physics [48] and astrophysics [56, 55, 41]. His analysis is also applicable to unstable interfacial motion in geophysical flows and internal gravity waves [61]. Extending the linear theory developed by Mikaelian, Liu et al. performed weakly nonlinear analysis for RMI with two interfaces in a three-layer fluid [33]. These studies treat an unbounded three-layer fluid. There also exists an analytical study for a bounded three-layer flow. Panda et al. [50] calculated the stable linear interfacial motion in a channel with bottom topography using the Fourier transform technique. There also exist some numerical studies for the motion of interfaces in a multi-layer fluid flow. Chen and Forbes [15] calculated the nonlinear behavior of steady periodic waves in a three-layer fluid with uniform shear in the middle layer using a numerical method of Galerkin-type. Zabusky and Zhang [63] investigated the shock inclined-curtain interaction of a planar RMI using the piecewise parabolic method (PPM) algorithm [17]. Lee and Kim presented the numerical result for the two-dimensional Kelvin-Helmholtz instabilities of multi-component fluids by directly solving the governing equations [31].

The theoretical analyses for the multi-layer fluid flows described above require daunting tasks, and it is almost impossible to perform such analytical calculations in the nonlinear regime. In order to investigate the motion of two interfaces in a three-layer fluid flow, we adopt the vortex sheet model (VSM) [1, 6, 4, 29, 30, 38] and calculate their nonlinear behavior numerically. It is known that VSM without the regularization of the singular integral, called the Birkhoff-Rott equation [9, 53, 54], provides the spectral accuracy (exponential accuracy) [57] if we adopt proper integral methods for spatial integration, such as the alternative point quadrature method [58]. By which, we can capture the nonlinear motion of the interfaces with analytical accuracy. On the other hand, VSM calculated with spectral accuracy is a purely mathematical model, and the result does not describe the real motion of the interfaces. As a model to describe the

more realistic long-time behavior of the unstable interfacial motion such as the roll-ups, the vortex (blob) method regularizing singular integrals [16, 30, 62, 18, 3, 7, 38, 37, 36] has been applied to various problems for the nonlinear evolution of interfaces. Unlike the physical regularizations such as the introduction of a vortex layer [8] or the surface tension effect [26, 34], the vortex method is mathematically proved that the solution obtained by the method uniformly converges to the Birkhoff-Rott equation as long as the initial condition is sufficiently smooth [as Eq. (21) adopted in the current study] [10, 14, 25]. The above studies by VSM treat the dynamics of a single interface in a two-layer flow. Extending the method of VSM to the motion of two interfaces in a three-layer RMI, Matsuoka succeeded in capturing the nonlinear interaction of two vortex sheets in a multi-component flow with density stratification [35]. This model is applicable to systems with any density differences. In the current study, we adopt the model equations developed in the above reference [35] and investigate the nonlinear behavior of unstable two interfaces in a three-layer fluid with uniform current.

We consider an unbounded three-layer fluid such that the lightest fluid is over the middle layer, and the heaviest fluid is set at the bottom layer, assuming that a uniform current exists in one of the three fluids. This kind of situation is often found in the flows with different temperatures in the ocean or atmosphere, where the lighter (heavier) fluid corresponds to the warmer (cooler) region. The initial conditions for numerical computations are determined by calculating the linear dispersion relation, in which the linear frequency is calculated using the Newton's method. The nonlinear interfacial motion with current in the upper layer is analogous to the one with current in the lower layer; however, the motion of interfaces with current in the middle layer is remarkably different from those two cases. As a result of the linear analysis, a varicose mode appears in this case. The varicose wave is a mode specific to two-interface systems, and it corresponds to a wave in which the upper and lower interfaces are 180° out of phase [61].

Varicose instabilities often appear in boundary-layer flows in transition from the laminar to turbulent flows [2, 11, 12, 13, 28, 51, 59]. Due to the shear flow between the wall and the laminar flow, the varicose instability develops to a complicated flow such as streaks with vortical structures [12, 22, 13]. These studies are mainly confined to the linear analysis or direct numerical simulations (DNS). In the current paper, we investigate the nonlinear development of the varicose instability using VSM. Unlike DNS, VSM can capture the finer structure of vortices in the instabilities. We consider the two-dimensional case; however, the flow structure caused by the varicose instability is analogous to that observed in the three-dimensional boundary-layer flows [22, 13]. By calculating the evolution of the velocity field, we reveal how the complicated interfacial structure in the varicose instability is formed.

This paper is organized as follows. In Section 2, we perform the linear analysis and derive the dispersion relations for using as the initial conditions of numerical calculations. In Section. 3, we overview the governing equations to describe the nonlinear dynamics of two interfaces in a three-layer fluid. In Section. 4, we present some numerical results
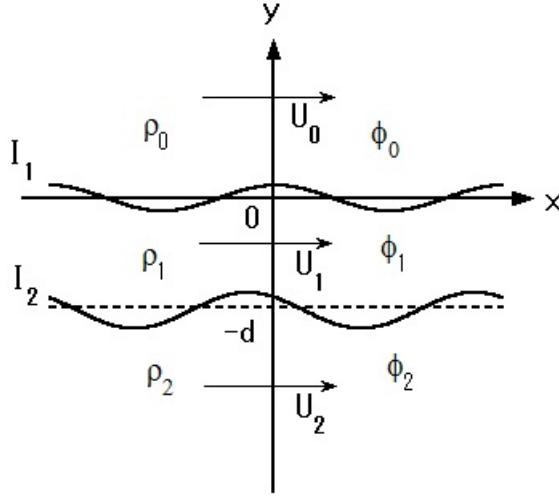
Figure 1. Schematic figure of the flow configurarion.

by VSM for three cases with different currents. Section 5 is devoted to conclusion.

2. The linear analysis

In this section, we perform the linear analysis and derive some dispersion relations as the initial conditions for numerical calculations. The governing equations adopted here [Eqs. (3) and (4) below] for the linear analysis are the same as those used in the reference [35] except the gravity term.

2.1. Dispersion relations

We consider two-dimensional inviscid and incompressible flows such that two fluid interfaces I_1 and I_2 with density stratification exist in it (Figure 1), where the undisterbed levels of I_1 and I_2 are set to $y = 0$ and $y = -d$ $(d > 0)$, respectively. The fluid motion is assumed to be irrotational except the interfaces I_1 and I_2. Then the velocity potential ϕ_i in the region i $(i = 0, 1, 2)$, which is related to the fluid velocity $\boldsymbol{u}_i$ as $\boldsymbol{u}_i = \nabla \phi_i$, satisfies the Laplace equation

$$\triangle \phi_i = 0, \quad (i = 0, 1, 2) \tag{1}$$

and the Bernoulli equation:

$$\rho_i \left[\frac{\partial \phi_i}{\partial t} + \frac{1}{2}(\nabla \phi_i)^2 + gy \right] + p_i = C_i(t), \quad (i = 0, 1, 2) \tag{2}$$

where ρ_i is the density of fluid i, p_i is the pressure, g is the gravitational acceleration, and $C_i(t)$ is a constant generally depending on time, which is determined from the boundary condition at I_i. By imposing the pressure continuous condition across the interfaces; $p_0 = p_1$ at I_1 $(y = 0)$ and $p_1 = p_2$ at I_2 $(y = -d)$, and taking into the hydrostatic pressure condition $p_i = C_i(t) - \rho_i gy$ $(i = 0, 1, 2, y = 0$ at I_1 and $y = -d$ at $I_2)$, we

obtain

$$C_1(t) = C_0(t) + (\rho_0 - \rho_1)gd, \quad C_2(t) = C_1(t) + (\rho_1 - \rho_2)gd.$$

Selecting $C_i(t) = C_i$, a constant, the Bernoulli equation (2) yields

$$\rho_i \left[\frac{\partial \phi_i}{\partial t} + \frac{1}{2}(\nabla \phi_i)^2 + gy \right]$$
$$= \rho_{i-1} \left[\frac{\partial \phi_{i-1}}{\partial t} + \frac{1}{2}(\nabla \phi_{i-1})^2 + gy \right] = 0, \quad (i = 1, 2). \tag{3}$$

We assume that the interfaces I_1 and I_2 are evaluated as the deviations $y = \eta_1(x, t)$ and $y = \eta_2(x, t)$ from the undisturbed levels $y = 0$ and $y = -d$ (Figure 1), respectively. Then the kinematic boundary conditions at interface I_i $(i = 1, 2)$ are given by

$$\frac{\partial \eta_1}{\partial t} - \frac{\partial \phi_i}{\partial y} = \frac{\partial \phi_i}{\partial x} \frac{\partial \eta_1}{\partial x} \quad (i = 0, 1) \quad \text{at } I_1,$$
$$\frac{\partial \eta_2}{\partial t} - \frac{\partial \phi_i}{\partial y} = \frac{\partial \phi_i}{\partial x} \frac{\partial \eta_2}{\partial x} \quad (i = 1, 2) \quad \text{at } I_2. \tag{4}$$

In the current study, we assume that each of the three fluid layers has a primary uniform velocity $U_i (i = 0, 1, 2)$. Linearizing the kinematic boundary condition (4) at the non-perturbative interfaces, we obtain the following linearized solutions for ϕ_i $(i = 0, 1, 2)$

$$\tilde{\phi}_0 = \Re[B_0 e^{-ky} e^{i(kx - \omega t)}] \quad (y > 0),$$
$$\tilde{\phi}_1 = \Re[(B_{11} e^{ky} + B_{12} e^{-ky}) e^{i(kx - \omega t)}] \quad (-d \leq y \leq 0), \tag{5}$$
$$\tilde{\phi}_2 = \Re[B_2 e^{ky} e^{i(kx - \omega t)}] \quad (y < -d),$$

and the vertical displacements of the interfaces at $y = 0$ and $y = -d$

$$\tilde{\eta}_1 = \Re[a_1 e^{i(kx - \omega t)}], \quad \tilde{\eta}_2 = \Re[a_2 e^{i(kx - \omega t)}], \tag{6}$$

where k is the wavenumber, ω is the linear frequency of the system, and we denote the first order quantities with tilde. Here, we assume that the amplitude a_1 is real. The coefficients B_0, B_{11}, B_{12}, and B_2 in (5) are given as

$$B_0 = \Re \left[\frac{i(\omega - kU_0)}{k} a_1 \right],$$
$$B_{11} = \Re \left[\frac{i(\omega - kU_1)}{k(e^{kd} - e^{-kd})}(a_1 - a_2 e^{-kd}) \right],$$
$$B_{12} = \Re \left[\frac{i(\omega - kU_1)}{k(e^{kd} - e^{-kd})}(a_2 - a_1 e^{kd}) \right], \tag{7}$$
$$B_2 = \Re \left[-\frac{i(\omega - kU_2)}{k} a_2 \right].$$

Taking into the uniform velocities U_i $(i = 0, 1, 2)$ and the equilibrium position of the interfaces, the velocity potential ϕ_i $(i = 0, 1, 2)$ and the displacement η_i $(i = 1, 2)$ are provided as

$$\phi_i = \tilde{\phi}_i + U_i x \quad (i = 0, 1, 2)$$
$$\eta_1 = \tilde{\eta}_1, \quad \eta_2 = \tilde{\eta}_2 - d \tag{8}$$
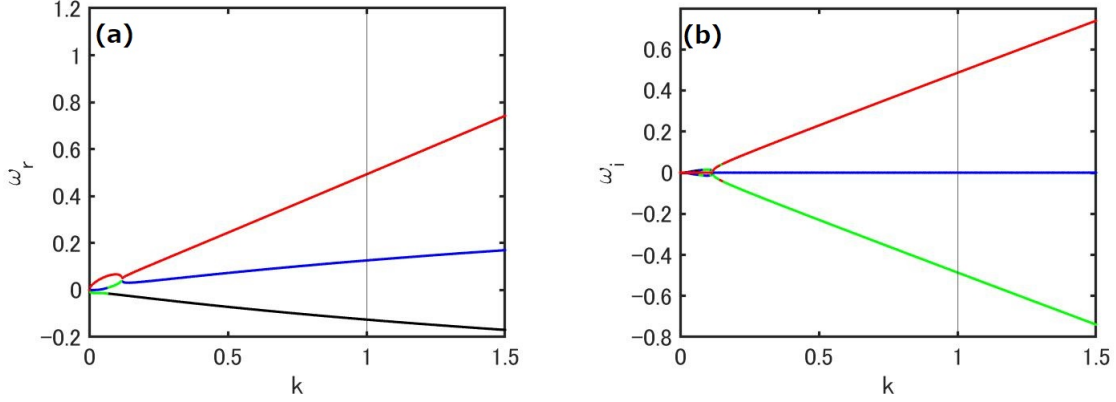
Figure 2. The (a) real and (b) imaginary parts of the dispersion curve in Case I given by (13), where the uniform velocities are $U_0 = 1$, $U_1 = 0$, and $U_2 = 0$. The densities are $\tilde{\rho}_0 = 0.99$ and $\tilde{\rho}_2 = 1.05$. The four branches ω_1 (black), ω_2 (blue), ω_3 (green), and ω_4 (red) are depicted in different colors. The vertical lines denote $k = 1$, the value selected for the numerical calculations in Section 4.
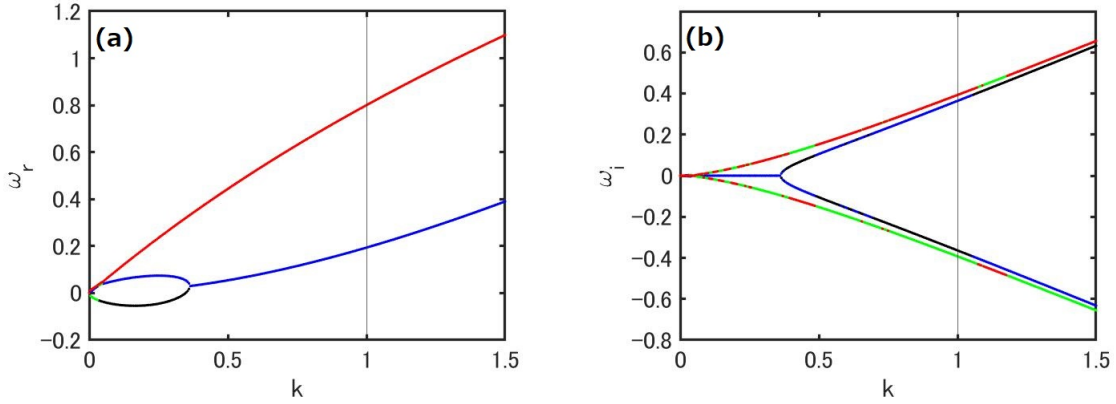

Figure 3. The (a) real and (b) imaginary parts of the dispersion curve in Case II given by (13), where the uniform velocities are $U_0 = 0$, $U_1 = 1$, and $U_2 = 0$ ($\tilde{\rho}_0 = 0.99$ and $\tilde{\rho}_2 = 1.05$). The colors are the same as Figure 2. The vertical lines denote $k = 1$ (refer to Section 4).

within the linear theory.

Linearizing the Bernoulli equation (3) at the undisturbed level $y = 0$ and $y = -d$ and using the result of (7), we obtain the following dispersion relation

$$D(\omega, k) = -D_1(\omega, k) + \frac{\Lambda^2(\omega, k)}{D_2(\omega, k)} = 0, \tag{9}$$

where

$$D_1(\omega, k) = (\rho_1 - \rho_0)g - \frac{1}{k}\left[\rho_0(\omega - kU_0)^2 + \rho_1(\omega - kU_1)^2 \coth(kd)\right],$$

$$D_2(\omega, k) = (\rho_2 - \rho_1)g - \frac{1}{k}\left[\rho_2(\omega - kU_2)^2 + \rho_1(\omega - kU_1)^2 \coth(kd)\right],$$
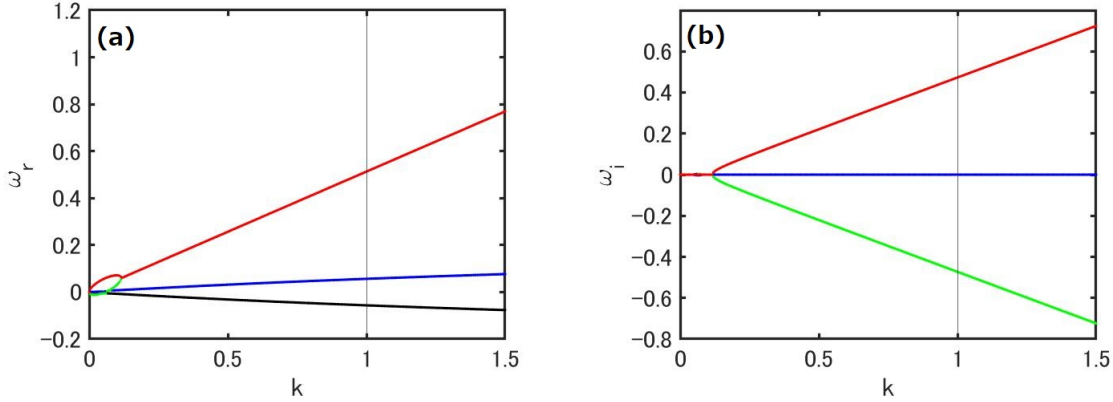
Figure 4. The (a) real and (b) imaginary parts of the dispersion curve in Case III given by (13) , where the uniform velocities are $U_0 = 0$, $U_1 = 0$, and $U_2 = 1$ ($\tilde{\rho}_0 = 0.99$ and $\tilde{\rho}_2 = 1.05$). The colors are the same as Figures 2 and 3. The vertical lines denotes $k = 1$ (refer to Section 4).

and

$$\Lambda(\omega, k) = \frac{\rho_1(\omega - kU_1)^2}{k \sinh(kd)}. \tag{10}$$

The linear dispersion relation (9) coincides with the result in the absence of the surface tention obtained by Craik and Adam [20]. The above calculations are also possible to perform using the Rayleigh equation [24]. Using the amplitude a_1, D_1, and Λ, the amplitude of a_2 in (6) is given by

$$a_2(\omega, k) = -\frac{D_1(\omega, k)}{\Lambda(\omega, k)} a_1. \tag{11}$$

The linear frequency ω is determined by solving the dispersion relation (9). Since $D(\omega, k) = 0$ in (9) is the fourth order equation with respect to ω; generally, four solutions exist in $D(\omega, k) = 0$ for a given k. We present the dispersion curves solved by the Newton's method in Figures 2 - 4, where $\omega = \omega_r + i\omega_i \in \mathbb{C}$ (ω_r, $\omega_i \in \mathbb{R}$). The calculations by the Newton's method are performed with tolerance level 10^{-12}. Here, we select the density ratio $\tilde{\rho}_i \equiv \rho_i/\rho_1$ ($i = 0, 2$), the initial amplitude a_1, the distance d, and the gravity g as

$$\tilde{\rho}_0 = 0.99, \quad \tilde{\rho}_2 = 1.05,$$
$$a_1 = 0.2, \quad d = 0.5, \quad g = 1, \tag{12}$$

where a_1 and d are normalized by the wavelength $L = 2\pi/k$ as $a_1/L \to a_1$ and $d/L \to d$, and the gravity g is normalized using the hydrostatic pressure as $gd\left[(\rho_0 - \rho_1) + (\rho_2 - \rho_1)\right]/(C_0 - C_2) \to g$ [5, 21]. The density ratios in (12) are selected as values close to those adopted by Craik and Adam [20], and Chen and Forbes [15]. The typical values of the density ratios are $0 < 1 - \tilde{\rho}_0 \ll 1$ and $0 < \tilde{\rho}_2 - 1 \ll 1$ in geophysical fluid dynamics or internal gravity waves; however, any values are possible
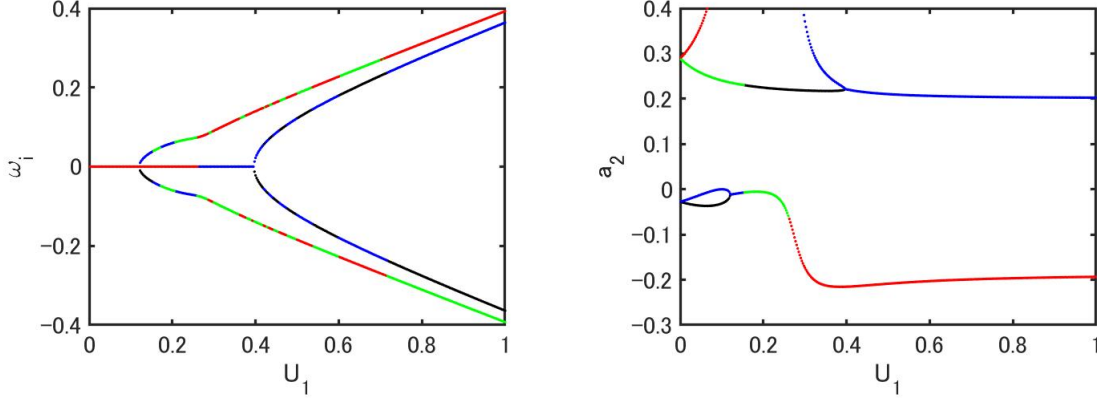
Figure 5. Varicose condition for various values of U_1, where the left and right figures denote ω_i and the real part of the amplitude a_2 versus U_1.

in plasma physics [43, 44, 45, 46, 33, 35]. We use the parameters (12) in the numerical calculations in Section 4 except Section 4.3.2, where smaller values of $|\tilde{\rho}_0|$ are adopted.

For the uniform velocities U_i $(i = 0, 1, 2)$, we consider the following three cases:

$$
\begin{aligned}
U_0 = 1, \quad U_1 = 0, \quad U_2 = 0, \quad &\text{(Case I)}, \\
U_0 = 0, \quad U_1 = 1, \quad U_2 = 0, \quad &\text{(Case II)}, \\
U_0 = 0, \quad U_1 = 0, \quad U_2 = 1. \quad &\text{(Case III)}.
\end{aligned} \tag{13}
$$

The four branches ω_1 (black), ω_2 (blue), ω_3 (green), ω_4 (red) in Figures 2 - 4 are depicted in colors. In Figure 2 (a), the branch ω_1 (black) coincides with ω_2 (blue) in the range of $0.015 < k \le 0.07$. The branch ω_2 takes the same value with ω_3 (green) in the range of $0.07 < k \le 0.12$, and finally, the branch ω_3 coincides with ω_4 (red) in the range of $0.12 < k \le 1.5$. In Figure 2 (b), the imaginary part of $\omega_3 = 0$ for $k < 0.07$, $\omega_4 = 0$ for $k < 0.12$, the branch $\omega_1 = 0$ for $k \ge 0.07$, and $\omega_2 = 0$ for $k \ge 0.12$.

In Figure 3 (a), the branch ω_3 coincides with ω_4 in the range of $k \ge 0.05$, and the branch ω_1 coincides with ω_2 in the range of $k \ge 0.365$. In the imaginary part ω_i of Case II, one branch is frequently exchanged with another one, as found in Figure 3 (b). In Figure 4 (a), the branch ω_3 coincides with the branch ω_4 in the range of $k \ge 0.12$. In Figure 4 (b), all branches are zero for $k \le 0.045$, and the branches $\omega_1 = \omega_2 = 0$ for $k \ge 0.08$. The mode that the most unstable one; i.e., the mode having the largest positive imaginary part, is realized first. We adopt the mode that the largest imaginary part appears for $k = 1$ (vertical lines in Figures 2 - 4) and investigate the behavior of the solution in the nonlinear regime in Section 4.3.2. We mention that other modes including $\omega_i < 0$ also turn out to be unstable for a longer time than the above mode for all $k > 0$ in the current system.
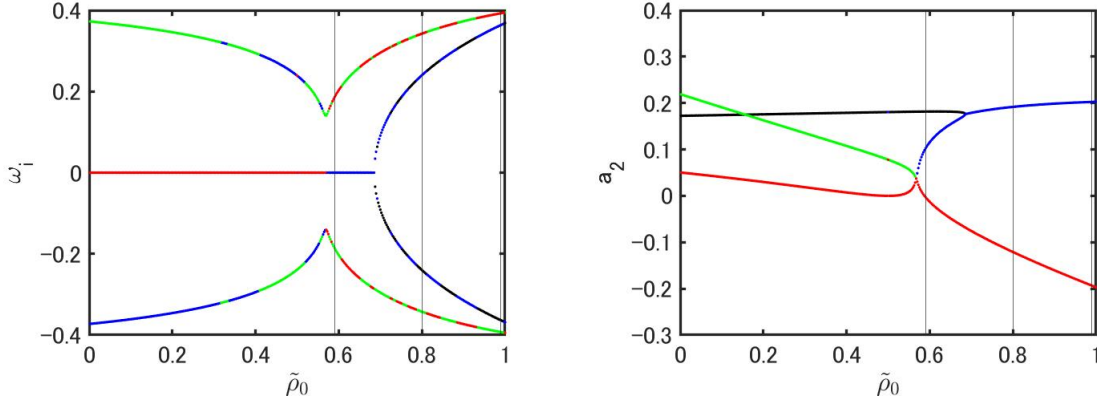
Figure 6. Varicose condition in Case II in (13) for various values of $\tilde{\rho}_0$, where the left and right figures denote ω_i and the real part of the amplitude a_2 versus normalized density $\tilde{\rho}_0$. The vertical lines denote $\tilde{\rho}_0 = 0.59$, 0.8, and 0.99, the values selected for the numerical calculations in Section 4.3.

2.2. Varicose mode

When the positive ω_i takes its maximum value in the four modes and the amplitude $\Re(a_2) < 0$ (out of phase condition), the varicose mode appears. This mode is the main topic of this article; therefore, we investigate that more specifically in this subsection. The varicose mode generally appears when $U_1 \neq 0$ such as Case II in (13). In the following, we fix the values of $\tilde{\rho}_2$, a_1, d, and g in (12) and adopt the wavenumber $k = 1$. The colors in Figures 5 and 6 are the same as those in Figures 2 - 4.

Figure 5 denotes the varicose condition obtained from the dispersion relation (9) for various values of U_1, where we set to $U_0 = U_2 = 0$. The vertical axis a_2 in the right figure denotes $\Re(a_2)$. When $U_1 > 0.12$, the varicose mode starts to appear in the branch ω_2 (blue), and when $U_1 > 0.26$, the mode shifts to the branches ω_3 (green) and ω_4 (red). When $U_1 = 0.22$, $\omega_r \sim kU_1$ ($\Lambda(\omega, k) \sim 0$) occurs; and therefore, the amplitude a_2 in (11) becomes extremely large. Figure 6 denotes the varicose condition in Case II obtained from the dispersion relation (9) for various values of $\tilde{\rho}_0$. As we see from Figure 6, when the normalized density $\tilde{\rho}_0$ is small, the varicose mode is hard to appear. When $\tilde{\rho}_0 > 0.585$, the varicose mode starts to appear mainly in the branch ω_4 (red) including the branch ω_3 (green) partially.

The varicose mode appears even in $U_0 \neq 0$ with $U_1 = 0$ or $U_2 \neq 0$ with $U_1 = 0$ such as Case I or III, at least in the linear stage for some values of U_0 or U_2 when we vary the wavenumber k. However, the maximum positive imaginary part $\omega_i \ll 1$ for these cases, and the varicose mode does not persist in the nonlinear regime as long as $U_1 = 0$. The result in Figure 6 is used in Section 4), does not occur.

3. Overview of the model formulation

In this section, we overview the governing equations to describe the dynamics of two interfaces in a three-layer fluid. A more detailed derivation for the model equations is provided in the references [35]. The formulation adopted here is based on the boundary integral method [57, 1, 35] developed to describe the motion of unstable interfaces such as vortex sheets [6, 4], in which the fluid velocity is provided by the vortex induced velocity called the Birkhoff-Rott equation [9, 53, 54]. The advantage of the vortex sheet model (VSM) is in the fact that physical quantities such as the velocity field or the velocity potential in the whole region are determined by only their initial boundary values. Therefore, we can significantly reduce the computational cost to calculate the flow field compared to the finite difference scheme or the spectral method.

We assume that the interfaces are L-periodic in the x direction, where L corresponds to the wavelength of the system given by the wavenumber k as $L = 2\pi/k$. We consider the interfaces $\boldsymbol{x} = \boldsymbol{X}_i$ $(i = 1, 2)$ without thickness and parameterize points on these interfaces as

$$\boldsymbol{X}_i(e, t) = [X_i(e, t), Y_i(e, t)]$$

using the same Lagrangian parameter e $(-L/2 \le e \le L/2)$. Now we consider the situation such that N_s $(N_s \in \mathbb{N})$ interfaces exist in the system. Since the system is described by the linear field (1), the (average) fluid velocity $\boldsymbol{W}$ at an arbitrary point $\boldsymbol{x} = (x, y)$ is presented by the superposition of the vortex induced velocities $\boldsymbol{W}_i$ $(i = 1, 2, \cdots, N_s)$ by the contribution from the interfaces I_i as

$$\boldsymbol{W} = \sum_{i=1}^{N_s} \boldsymbol{W}_i. \tag{14}$$

In the current study, $N_s = 2$. The vortex induced velocity $\boldsymbol{W}_i$ is given by

$$W_{i,x}(x, y) = -\frac{1}{2L} \int_{-L/2}^{L/2} \frac{\gamma_i(e', t) s_{i,e}(e', t) \sinh k(y - Y_i(e', t))}{\cosh k(y - Y_i(e', t)) - \cos k(x - X_i(e', t))} de',$$
$$W_{i,y}(x, y) = \frac{1}{2L} \int_{-L/2}^{L/2} \frac{\gamma_i(e', t) s_{i,e}(e', t) \sin k(x - X_i(e', t))}{\cosh k(y - Y_i(e', t)) - \cos k(x - X_i(e', t))} de', \tag{15}$$

where

$$\gamma_i = \boldsymbol{\gamma}_i \cdot \boldsymbol{t}_i = \partial \Gamma_i / \partial s_i, \quad (\boldsymbol{\gamma}_i = \boldsymbol{u}_i - \boldsymbol{u}_{i-1}) \tag{16}$$

denotes the (true) vortex sheet strength of interface I_i derived from the circulation $\Gamma_i \equiv \phi_i - \phi_{i-1}$, in which s_i is the arc length, and $\boldsymbol{t}_i$ is the unit tangent of the interface I_i, respectively. The subscript e denotes the differentiation with respect to e and $s_{i,e} = \sqrt{X_{i,e}^2 + Y_{i,e}^2}$. The integral (15) becomes the principal value integral in case that the point $\boldsymbol{x} = (x, y)$ is on the interface I_i; i.e., $(x, y) = (X_i, Y_i)$ [35].

There is an arbitrariness for the selection of the tangential velocity on an interface [6, 26]. Taking this into account, we define the interfacial velocity $\boldsymbol{u}_i^+$ at each interface I_i labelled by the Lagrange parameter e as

$$\boldsymbol{u}_i^+ = \boldsymbol{W}|_{\boldsymbol{x} = \boldsymbol{X}_i} - \frac{A_i}{2} \boldsymbol{\gamma}_i, \tag{17}$$

where A_i is the Atwood number that denotes the density ratio between fluids i and $i-1$ $(i = 1, 2, \cdots N_s)$, which is defined by

$$A_i = \frac{\rho_{i-1} - \rho_i}{\rho_{i-1} + \rho_i}. \tag{18}$$

It should be noted that the second term on the right-hand side of (17) only contributes to the tangential component of the velocity $\boldsymbol{u}_i^+$. The interfacial velocity (17) gives a weighted average between the fluid velocity $\boldsymbol{u}_i$ and $\boldsymbol{u}_{i-1}$ [35]. Supposing the temporal evolution of $\boldsymbol{X}_i$ is provided by $\boldsymbol{u}_i^+$ in the Lagrange frame, we obtain the relation

$$\frac{\mathbf{d}X_i}{\mathrm{d}t} = \boldsymbol{u}_i^+, \quad \frac{\mathrm{d}}{\mathrm{d}t} = \frac{\partial}{\partial t} + \boldsymbol{u}_i^+ \cdot \nabla, \tag{19}$$

where $\mathrm{d}/\mathrm{d}t$ denotes the Largange derivative moving with the velocity $\boldsymbol{u}_i^+$.

From now on, we fix the number of interfaces N_s as $N_2 = 2$. Selecting $y = Y_i$ $(i = 1, 2)$ into the Bernoulli equation (3) and differentiating that with respect to e, we obtain the evolution equation for the sheet strength γ_i [35]

$$\frac{\mathrm{d}\gamma_i}{\mathrm{d}t} = \frac{2A_i}{s_{i,e}} \left(X_{i,e} \frac{\mathrm{d}W_{i,x}}{\mathrm{d}t} + Y_{i,e} \frac{\mathrm{d}W_{i,y}}{\mathrm{d}t} \right) - \frac{(1 - A_i^2)\gamma_i}{s_{i,e}^2} (X_{i,e} W_{i,x,e} + Y_{i,e} W_{i,y,e})$$
$$+ \frac{3A_i}{2s_{i,e}} (\gamma_i^2)_e - \frac{A_i^2}{s_{i,e}} (\gamma_{i,e} T_i + \gamma_i T_{i,e}) + \frac{2A_i g Y_{i,e}}{s_{i,e}}, \tag{20}$$

where $T_i = \boldsymbol{t}_i \cdot \boldsymbol{W}_i$. We mention that an artificial parameter $\tilde{\alpha}$ [38, 41, 35] to control the tangential velocities of interfaces is not necessary for the current system due to the existence of the linear terms (the uniform current and the gravity term) and the small Atwood numbers $|A_i| \ll 1$ in (18). The former terms stabilize the calculations, and the latter works for the convergence. Due to the absence of the artificial parameter, some coefficients in (20) are different from those in the evolution equation of γ_i in the reference [35]. Solving (19) and (20) simultaneously by taking (14) and (15) into account, we can determine the motion of interfaces I_1 and I_2.

4. Numerical results

In this section, we present the numerical results by the model equations provided in the previous section Section 3. The initial conditions for the three-layer flow are determined by (8), setting $t = 0$ in (5) and (6), where the frequency ω and the initial amplitude a_2 are provided by the dispersion relation (9) and (11), respectively. Here, we set the initial conditions of the interface (X_i, Y_i) and γ_i $(i = 1, 2)$ as

$$X_i = e, \quad Y_1 = a_1 \cos ke, \quad Y_2 = \Re \left(a_2 e^{ike} \right),$$
$$\gamma_1 = \Re \left(\frac{\partial \phi_1}{\partial x} - \frac{\partial \phi_0}{\partial x} \right)_{\substack{t=0 \\ x=e \\ y=0}}, \quad \gamma_2 = \Re \left(\frac{\partial \phi_2}{\partial x} - \frac{\partial \phi_1}{\partial x} \right)_{\substack{t=0 \\ x=e \\ y=-d}}, \tag{21}$$

where a_1 is given by (12). The most unstable mode, i.e., the mode that its imaginary part is maximal for a fixed wavenumber k in the linear dispersion curves, is selected for numerical calculations.
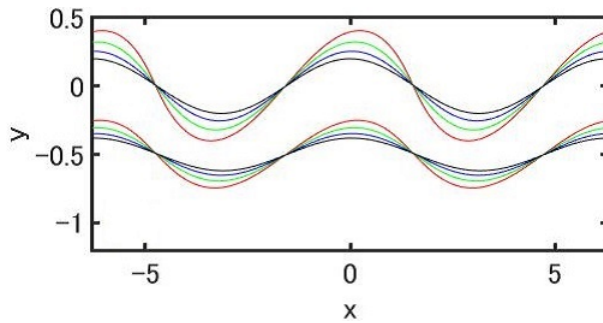
Figure 7. Interfacial structures for Case I without regularization. The colors in the figure denote $t = 0$ (black), $t = 0.5$ (blue), $t = 1.0$ (green), and $t = 1.5$ (red), respectively. A period of two wavelengths is depicted in the figures.

In numerical calculations, we adopt the alternative point quadrature method [58] for the calculation of the principal value integral $P(e)$ with integrand $f(e, e')$

$$P(e_j) = \frac{2h}{2L} \sum_{\substack{m=0 \\ m \neq j = odd}}^{N-1} f(e_j, e_m),$$

which appears in (15) and (20) when $(x, y) = (X_i, Y_i)$, where $e_j = jh$ is the discretization of e and $h = L/N$, N the grid number. For the contribution from the other interface I_j $(i \neq j)$, the conventional trapezoidal rule is adopted. The temporal integration is calculated using the fourth-order Runge-Kutta scheme, and the simultaneous Fredholm equations of the second kind (20) is solved by iteration with tolerance level 10^{-12}.

For more details of the numerical method, refer to the reference [35]. For the calculation by VSM with regularization [39, 40, 35], which indicates that we insert a finite regularized parameter δ^2 (this δ is often called Krasny's δ) into the denominators of the singular integrals (15) [30]. It is reported that $\delta = 0.1 - 0.2$ well describes experimental results [38, 49]. We select the value of δ as $\delta = 0.1$ throughout this section when $\delta \neq 0$. The calculations by the other values of δ are provided in Appendix Appendix A for comparison. For the calculations without regularization, which indicates $\delta = 0$, we select the number of grid points N discretizing on the interfaces as $N = 512$, and the time step $\triangle t$ as $\triangle t = 2.5 \times 10^{-3}$ throughout this section. The calculations with regularization $(\delta = 0.1)$ in Sections 4.1 (Case I) and 4.2 (Case III) are perfomed with $N = 1024$ and the time step $\triangle t$ as $\triangle t = 1.25 \times 10^{-3}$, while the calculations with regularization in Section 4.3 are performed with $N = 2048$ and the time step $\triangle t = 6.25 \times 10^{-4}$ to capture the fine structure of the interfaces. We fix the wavenumber of the initial perturbation as $k = 1$ in the numerical calculations. The parameters (12) are adopted for all calculations in the following subsections excluding Section 4.3.2, in which another values of $\tilde{\rho}_0$ are adopted (other parameters are the same). The variables x, y, and t are normalized as $kx \to x$, $ky \to y$, and $|\omega_r|t \to t$ in the following numerical calculations. The vortex sheet strength γ_i $(i = 1, 2)$ in Case I, II, and III [refrer to (13)] are normalized by the shear velocity U_j $(j = 0, 1, 2)$ as $\gamma_i/U_j \to \gamma_i$ for each case.
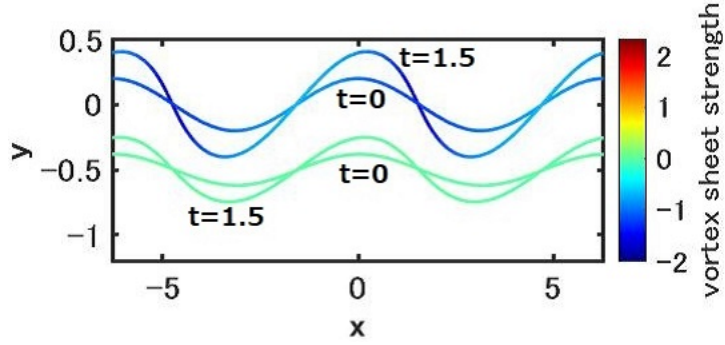
Figure 8. Vortex sheet strengths γ_1 and γ_2 corresponding to the interfacial structures in Figure 7, where $t = 0$ and $t = 1.5$ are depicted.
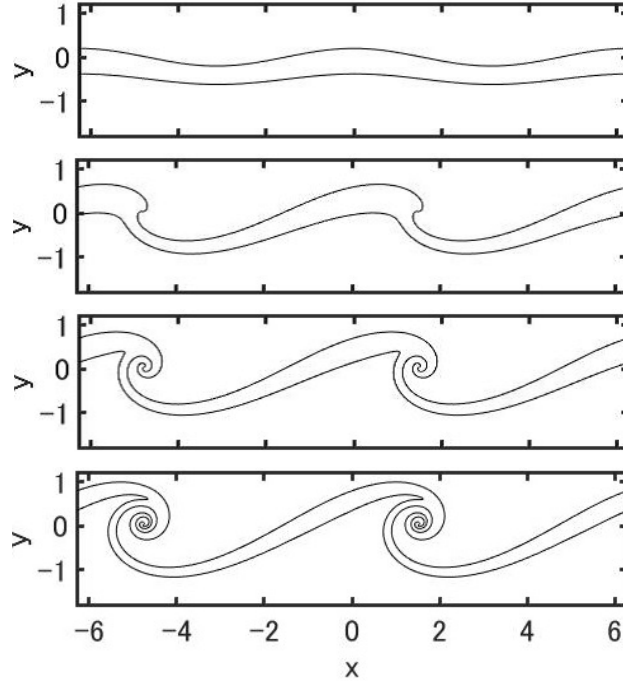

Figure 9. Interfacial structures for Case I with regularization. The panels show $t = 0,\ 3,\ 4,\ 5$ from the top to the bottom. A period of two wavelengths is depicted in the figures.

4.1. Nonlinear interfacial motion with current in the upper layer (Case I)

In this subsection, we present the numerical results for Case I in (13). The imaginary part ω_i takes its largest value in the branch ω_4 [the red curve in Figure 2 (b)] for the wavenumber $k = 1$. Therefore, we take this branch as the initial condition. Then the linear frequency $\omega(k) \in \mathbb{C}$ and the initial amplitude $a_2(k) \in \mathbb{C}$ are given by

$$\omega(1) = 0.4927047 + 0.4859008i,$$
$$a_2(1) = -0.0038787 + 0.1193469i,$$
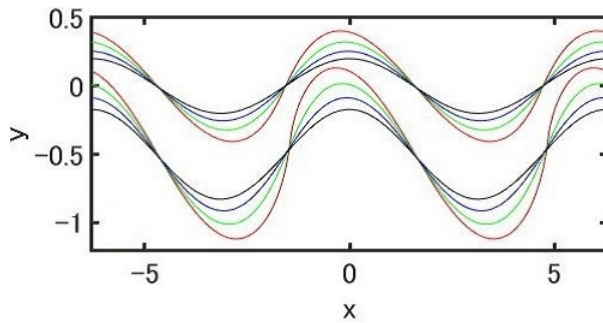
(22)

for $a_1 = 0.2$.

Figure 10. Interfacial structures for Case III without regularization. The colors in the figure denote $t = 0$ (black), $t = 0.5$ (blue), $t = 1.0$ (green), and $t = 1.5$ (red), respectively (same as Figure 7). A period of two wavelengths is depicted in the figures.

We present the temporal evolution of two interfaces calculated by VSM without regularization in Figure 7. The interfaces propagate from left to right, increasing their amplitudes. The interfacial shapes are asymmetric due to the density stratification, and the deformation of the upper interface I_1 is larger than that of the lower interface I_2. This asymmetricity is enhanced in the long-time behavior by the calculation with regularization (refer to Figure 9). The calculation without regularization breaks down at around $t = 1.8$ due to the occurrence of curvature singularity [47]. Figure 8 shows the interfacial structures for $t = 0$ and $t = 1.5$ with the colored scale of the vortex sheet strengths γ_1 and γ_2. For Case I, the sheet strength γ_1 takes negative values over $0 \leq t \leq 1.5$, while the sheet strength $|\gamma_2| \sim 0$ within this time range. This suggests that the vorticity is not induced on the interface that is not directly affected by the velocity shear.

We show the temporal evolution of two interfaces calculated by VSM with regularization in Figure 9. The regularization enables us to perform the long-time computations beyond the curvature singularity. When $t \geq 3$, the roll-up of the interfaces associated with the Kelvin-Helmholtz instability (KHI) appears, and the two interfaces approach each other. These interfaces merge and behave like a single vortex sheet at the last computed stage $t = 5$. A similar phenomenon is also observed in the incompressible multi-layer RMI [35]. When the roll-up begins, the interfaces hardly propagate, and the wave energy is available for the roll-up. Since the vortex sheet strength $|\gamma_1| > |\gamma_2|$, the roll-up of I_1 is stronger than that of I_2, which generates the asymmetricity in the interfacial structure.

4.2. Nonlinear interfacial motion with current in the lower layer (Case III)

In this subsection, we present the numerical results for Case III in (13). The imaginary part ω_i takes its largest value in the branch ω_4 [the red curve in Figure 4 (b)] for $k = 1$. We take this branch as the initial condition. Then the linear frequency $\omega(k)$ and the
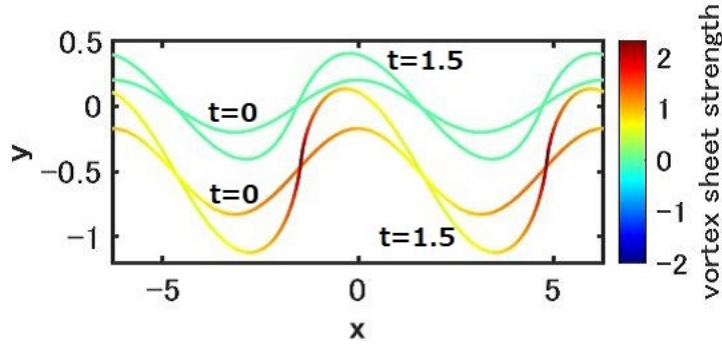
Figure 11. Vortex sheet strengths γ_1 and γ_2 corresponding to the interfacial structures in Figure 10, where $t = 0$ and $t = 1.5$ are depicted.
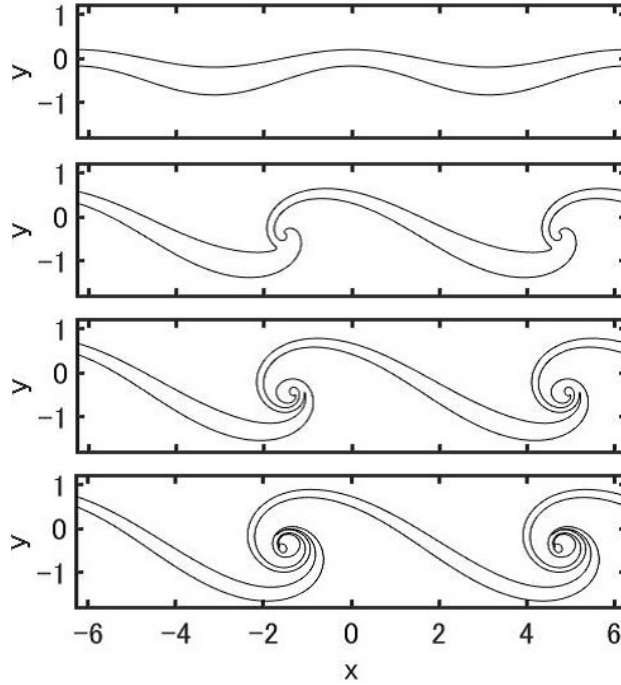

Figure 12. Interfacial structures for Case III with regularization. The panels show $t = 0, 3, 4, 5$ from the top to the bottom. A period of two wavelengths is depicted in the figures.

initial amplitude $a_2(k)$ are given by

$$\begin{aligned}
\omega(1) &= 0.5131064 + 0.4728463i, \\
a_2(1) &= 0.3285275 + 0.0021335i,
\end{aligned} \tag{23}$$

for $a_1 = 0.2$.

We present the temporal evolution of two interfaces calculated by VSM without regularization in Figure 10. The behavior of the interfaces in Case III is analogous to that in Case I, although the direction of the growth is the opposite. This growth direction is determined by the sign of the vortex sheet strength induced on the governing
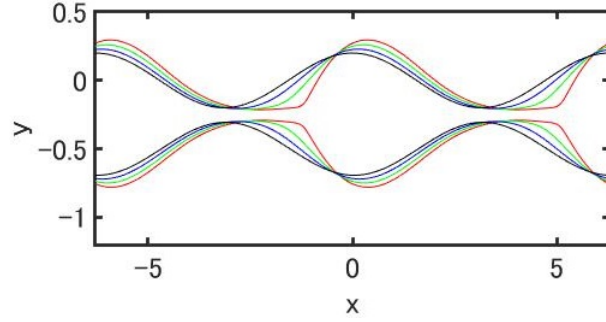
Figure 13. Interfacial structures for Case II without regularization. The colors in the figure denote $t = 0$ (black), $t = 0.25$ (blue), $t = 0.5$ (green), and $t = 0.75$ (red), respectively. A period of two wavelengths is depicted in the figures.
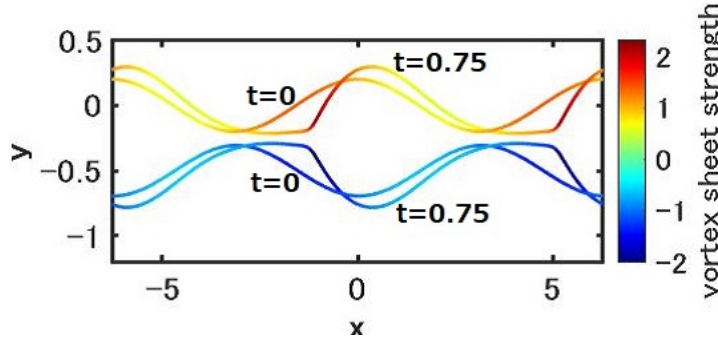

Figure 14. Vortex sheet strengths γ_1 and γ_2 corresponding to the interfacial structures in Figure 13, where $t = 0$ and $t = 0.75$ are depicted.

interface, which is I_1 in Case I and I_2 in Case III (refer to Figures 8 and 11). The interfacial structures for $t = 0$ and $t = 1.5$ with the colored scale of the vortex sheet strengths γ_1 and γ_2 are depicted in Figure 11. Contrary to Case I (Figure 8), the sheet strength γ_2 takes positive values over $0 \leq t \leq 1.5$, while the sheet strength $|\gamma_1| \sim 0$ within this time range. This reflects the fact that the vorticity is not induced on the upper interface I_1 that is not directly affected by the velocity shear in the lower layer.

Figure 12 shows the temporal evolution of two interfaces calculated by VSM with regularization. A similar roll-ups as Figure 9 are found in this figure, although the direction of the roll-up is opposite to the one in Case I. Since the vortex sheet strength $|\gamma_2| > |\gamma_1|$, the roll-up of I_2 is stronger than that of I_1 in Case III, contrary to Case I. We mention that the sheet strengths $|\gamma_1|$ and $|\gamma_2|$ in Case I and Case III are considerably smaller than those in Case II (refer to Section 4.3) even after the roll-up occurs.

4.3. Nonlinear interfacial motion with current in the middle layer (Case II) -varicose instabilities-

In this subsection, we present the numerical results for Case II in (13). The parameters in (12) are maintained throughout this subsection except the value of $\tilde{\rho}_0$.
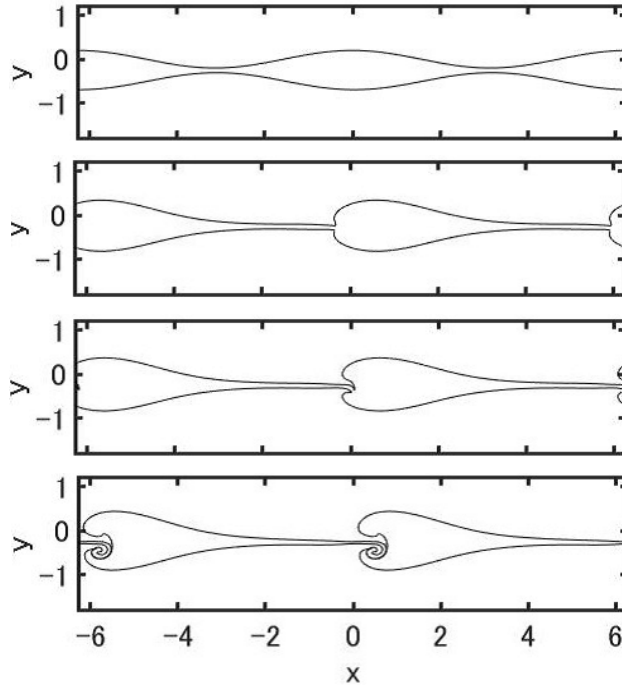
Figure 15. Interfacial structures for Case II with regularization. The panels show $t = 0$, 1.3, 1.5, 2 from the top to the bottom. A period of two wavelengths is depicted in the figures.

4.3.1. Varicose structure of interfaces with small density stratification In this sub-subsection, we investigate the case with the same value of $\tilde{\rho}_0$ ($\tilde{\rho}_0 = 0.99$) as the above two subsections 4.1 and 4.2. The imaginary part ω_i takes its largest value in the branch ω_4 [the red curve in Figure 3 (b)] for $k = 1$. We take this branch as the initial condition. Then the linear frequency $\omega(k)$ and the initial amplitude $a_2(k)$ are given by

$$\omega(1) = 0.8001652 + 0.3926127i,$$
$$a_2(1) = -0.1934602 + 0.0080392i,$$
(24)

for $a_1 = 0.2$. This initial amplitude a_2 gives the varicose wave. The imaginary part of a_2 is extremely small but not zero; therefore, the initial configuration of two interfaces is not symmetric perfectly. This asymmetricity is enhanced in the subsequent evolution of the interfaces. We mention that even if the imaginary part of a_2 is zero and the initial configuration of two interfaces is symmetric, the nonlinear evolution of the interfaces becomes asymmetric as long as the density stratification exists. We provide the interfacial structures in the absence of the density stratification in Appendix Appendix B for reference.

Figure. 13 shows the temporal evolution of two interfaces calculated by VSM without regularization. The varicose wave at $t = 0$ gradually steepens at one end, and a teardrop-shaped wave appears at $t = 0.75$. The asymmetricity of the interfacial shapes between I_1 and I_2 is not noticeable for $0 \le t \le 0.75$. The calculation without regularization breaks down at around $t = 0.9$, accompanied by the occurrence of
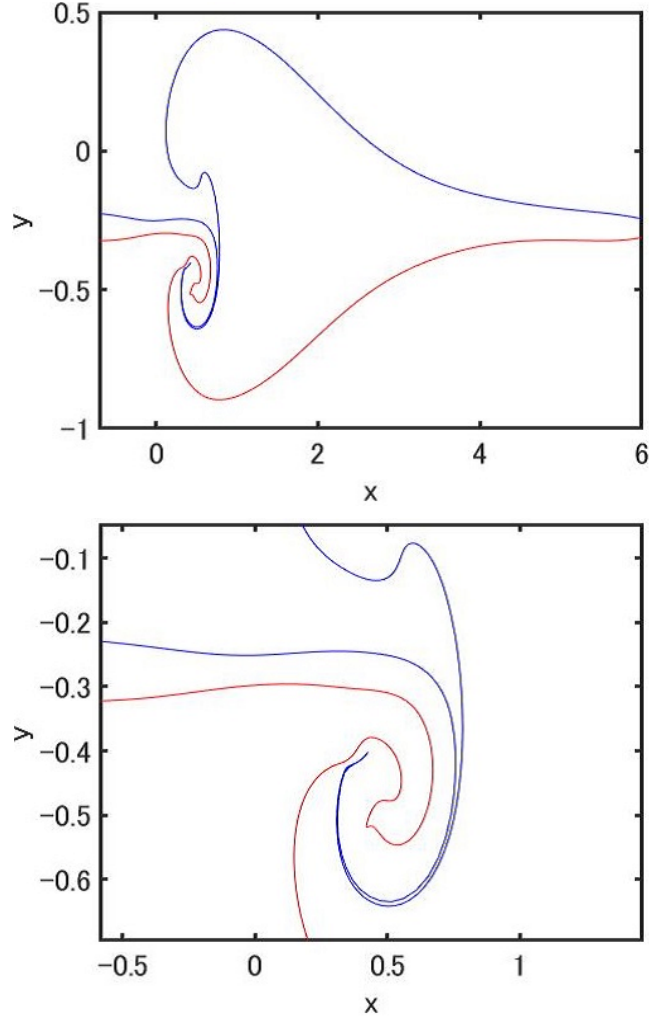
Figure 16. Enlarged view of the interfacial structure at $t = 2$ in Figure 15, where the blue and red lines denote the upper interface I_1 and the lower interface I_2, respectively. The neighborhood of the roll-up in the upper figure is further magnified in the lower figure.

curvature singularity. We show the interfacial structures for $t = 0$ and $t = 0.75$ with the colored scale of the vortex sheet strengths γ_1 and γ_2 in Figure 14. For Case II, considerably strong sheet strengths are induced on both interfaces, in which γ_1 possesses a positive sign, and γ_2 possesses a negative sign.

We present the temporal evolution of two interfaces calculated by VSM with regularization in Figure 15. When $t = 1.3$, the asymmetricity begins to appear between the interfacial shapes I_1 and I_2, which is enhanced further as time passes. The steepening end found in Figure 13 becomes unstable, and multivaluedness appears in the interfaces. When $t \geq 1.5$, the roll-up begins to appear in the interfacial structure, and a heart-shaped vortex sheet is formed at $t = 2$. The similar structure as found in Figure 15 is also observed in the experiment for a boundary-layer flow past a cylindrical roughness element [13]. In order to observe the fine structure of the roll-up, we present the enlarged
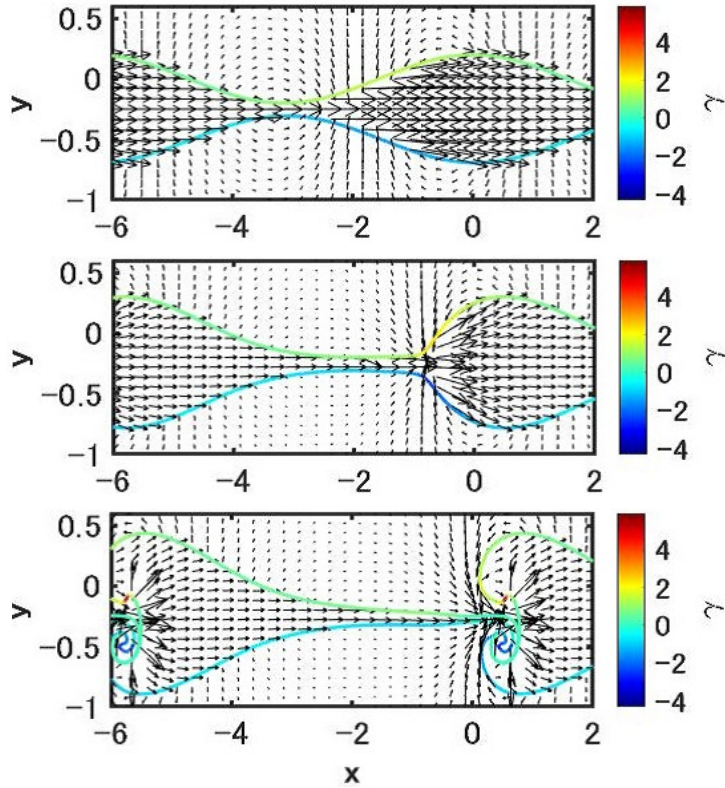
Figure 17. Interfacial structures with the colored scale of the vortex sheet strengths and the velocity fields in Case II, where $t = 0, 1, 2$ from the top to the bottom.

view of the lowest panel ($t = 2$) of Figure 15 in Figure 16. This structure cannot capture accurately in lower resolution, such as Case I and III. The stronger sheet strengths than those in Case I and III (refer to Figures 9 and 12) are induced at the tips of the roll-up in Figure 16 at the late stage of computations.

Figure 17 shows the interfacial structures and the velocity fields for Case II. The velocity field is calculated from (15) [41, 35, 40]. In the varicose mode, a kind of two-dimensional deformable nozzle is formed at $t = 0$. A high-speed fluid ejects from the throat in the nozzle like a jet, and a large shear caused by the velocity difference between inside and outside of an interface is gradually formed in the neighborhood of the narrowest part of the throat ($t = 1$ and 2). This shear induces the vorticity, and therefore, a strong vortex sheet strength appears around the outlet of the nozzle, which leads to a heart-shaped vortex sheet. This is a typical nozzle jet flow except the deformation of the interfaces, and a similar flow structure is also found in the boundary layer streaks [2, 13, 51].

As found in Figure 5, the varicose mode appears even for the smaller values of U_1 when we fix the other parameter values. We mention that the interfacial shapes with these values of U_1 have almost the same structure as that of Case II obtained in this sub-subsection when the regularized parameter δ is identical.
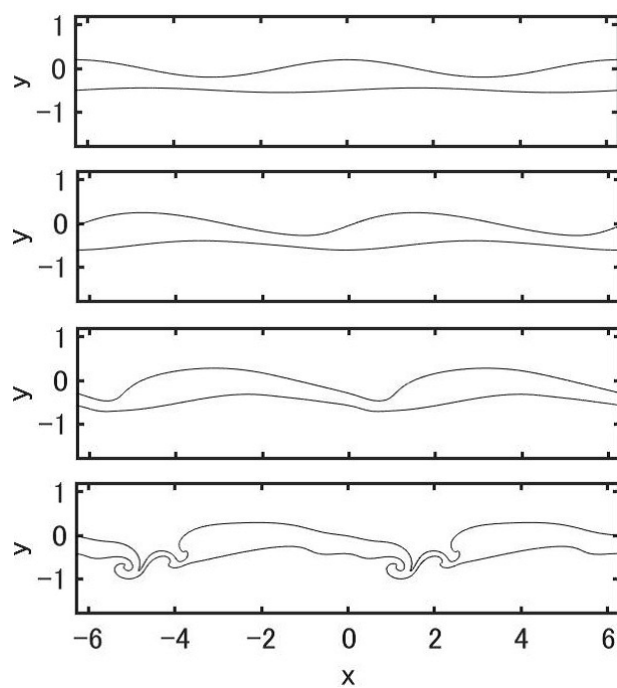
Figure 18. Interfacial structures for Case II with $\tilde{\rho}_0 = 0.59$. The panels show $t = 0, 2, 4, 6$ from the top to the bottom.
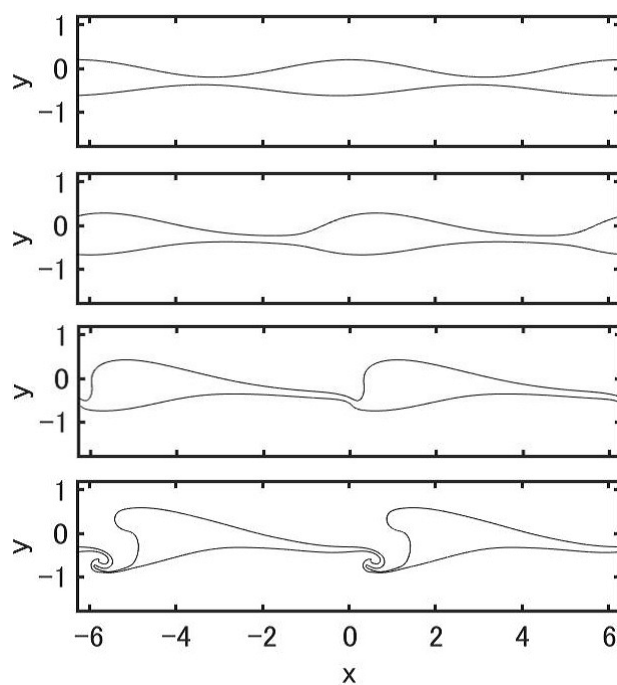

Figure 19. Interfacial structures for Case II with $\tilde{\rho}_0 = 0.8$. The panels show $t = 0, 1, 2, 3$ from the top to the bottom.

4.3.2. Other varicose interfacial structures -effects of density stratification- In this sub-subsection, we present the numerical results for Case II in (13) with different values of $\tilde{\rho}_0$ ($\tilde{\rho}_0 = 0.59$ and 0.8) from the caluculations in Section 4.3.1. All calculations in this sub-subsection (Figures 18 and 19) are regularized with $\delta = 0.1$. For both cases $\tilde{\rho}_0 = 0.59$ and $\tilde{\rho}_0 = 0.8$, the imaginary part ω_i takes its largest value in the branch ω_4 (the red curve in the upper figure in Figure 6). We take this branch as the initial condition. Then the linear frequency $\omega(k)$ and the initial amplitude $a_2(k)$ are given by

$$\begin{aligned} \omega(1) &= 0.7815345 + 0.185846i, \\ a_2(1) &= -0.0030102 - 0.0527351i, \end{aligned} \tag{25}$$

for $\tilde{\rho}_0 = 0.59$, and

$$\begin{aligned} \omega(1) &= 0.8149770 + 0.3423959i, \\ a_2(1) &= -0.1210145 - 0.0316079i, \end{aligned} \tag{26}$$

for $\tilde{\rho}_0 = 0.8$, respectively. The density $\tilde{\rho}_0 = 0.59$ is the value that the varicose mode starts to appear in the current parameters (refer to Figure 6).

Figure 18 shows the interfacial structures with $\tilde{\rho}_0 = 0.59$. When the density ratio $\tilde{\rho}_0$ is small, the initial value of $|\Re(a_2)|$ is extremely small, and in-phase modes arise in the higher harmonics, which disturbs the development to the varicose structure of the interfaces. The development of instability is relatively slow, and the heart-shaped structure as found in Section 4.3.1 does not appear for $\tilde{\rho}_0 = 0.59$. We present the temporal evolution of the interfaces with $\tilde{\rho}_0 = 0.8$ in Figure 19. The development of instability is also slow compared to $\tilde{\rho}_0 = 0.99$ in Section 4.3.1, and the heart-shaped structure is not found even in this value of $\tilde{\rho}_0$. We mention that it is $\tilde{\rho}_0 > 0.95$ that the similar interfacial structure as Figure 15 starts to appear.

5. Conclusion

This study has presented nonlinear motions of unstable two interfaces in a three-layer fluid with uniform current and density stratification. We have investigated the temporal evolutions of the interfaces for three cases such that the uniform current is present in the upper, middle, and lower layers, respectively. The initial conditions for numerical computations were provided by the linear analysis, in which the dispersion relations were calculated by the Newton's method. Taking the most unstable mode in the dispersion curves as the initial condition, we investigated the nonlinear evolution of the two interfaces numerically using VSM with and without regularizations. For the case that the uniform current was present in the lower layer, the nonlinear behavior of the interfaces resembled the one for the case that the current was present in the upper layer, in which the interface with current rolled up, involving the other interface apart from the current in the roll-up. The two interfaces merged at the late stage of computations using VSM with regularization, and, finally, they behaved like a single vortex sheet.

On the other hand, the nonlinear evolution of the interfaces when the current was present in the middle layer was quite different from the above two cases. In this case, a varicose mode appeared as the initial wave regardless of the wavenumber. When the initial varicose wave became unstable, it developed into a teardrop-shaped wave, and finally, an asymmetric heart-shaped vortex sheet was formed at the last computed stage of the calculation by VSM with regularization. The instability in the varicose wave was stronger than that in the above two cases , and an intense concentration of the vortex sheet strength; i.e., the concentration of vorticity occurred at the center of the roll-up. The heart-shaped structure is formed by a high-speed flow ejecting from the narrowest part of the throat like a nozzle jet. The interfacial structure is almost unchanged even though the magnitude of the shear velocity U_1 is varied, as long as the shear velocity exists in the middle layer and the density ratio ρ_0/ρ_1 is close to 1. On the other hand, the varicose structures with smaller density ratios ρ_0/ρ_1 do not form the heart-shaped vortex sheet even if the shear velocity in the middle layer has a sufficiently large value. We mention that the density ratios adopted in Section 4.3.2 are the values that are not realized in geophysical fluid dynamics and internal gravity waves, but those are possible in plasma physics.

The varicose mode plays an important role even in multi-component planar liquid sheets [27, 32], in which the varicose instability causes the eventual breakup of a liquid sheet at full-wavelength intervals of the fundamental wave. The obtained results in the current study may give some knowledge to that field. As we see from Fig. 5 (b), the real part of the amplitude a_2 diverges at $U_1 \sim 0.2175$ for a fixed $k = 1$. Similar divergence is also observed for $k \sim 0.048$ when we fix the shear as $U_1 = 1$ (Case II). In the neighborhood of these parameter values, numerical calculations immediately break down. This suggests that the solutions in multi-layer flows (at least in varicose mode) do not always exist for all d, k and U, although how such singular solutions appear in nature or experiments are unknown.

Acknowledgments

Appendix A. Dependence on the regularized parameter

We present the interfacial structures at the last computed stage with various regularized parameter δ in Figure 20, where all parameters are the same as those in Section 4.3.1, and the calculations are performed with $N = 2048$ and the time step $\triangle t = 6.25 \times 10^{-4}$. As the regularized parameter δ becomes smaller, the roll-up becomes stronger, and it
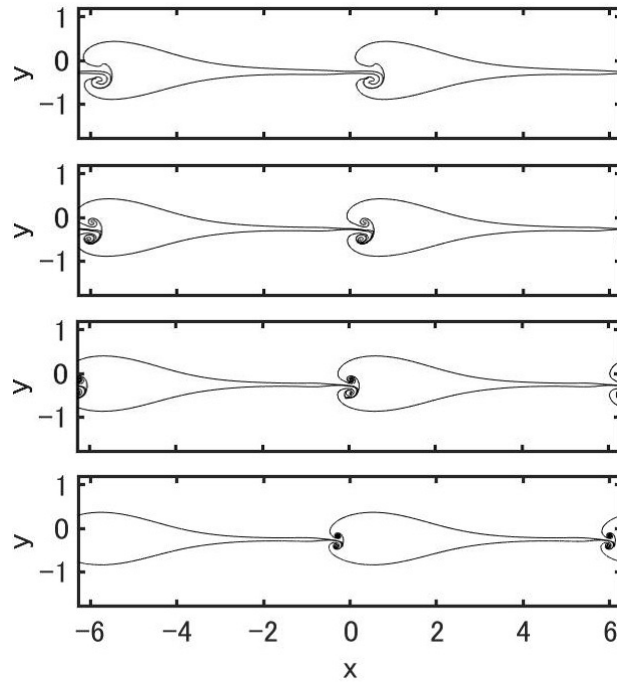
Figure 20. Interfacial structures at the last computed stage in Case II with various regularized parameter δ, where $\tilde{\rho}_0 = 0.99$. The panels show $t = 2$ with $\delta = 0.1$, $t = 1.75$ with $\delta = 0.05$, $t = 1.5$ with $\delta = 0.025$, and $t = 1.25$ with $\delta = 0.0125$ from the top to the bottom. The top panal coincides with the lowest panel in Figure 15.
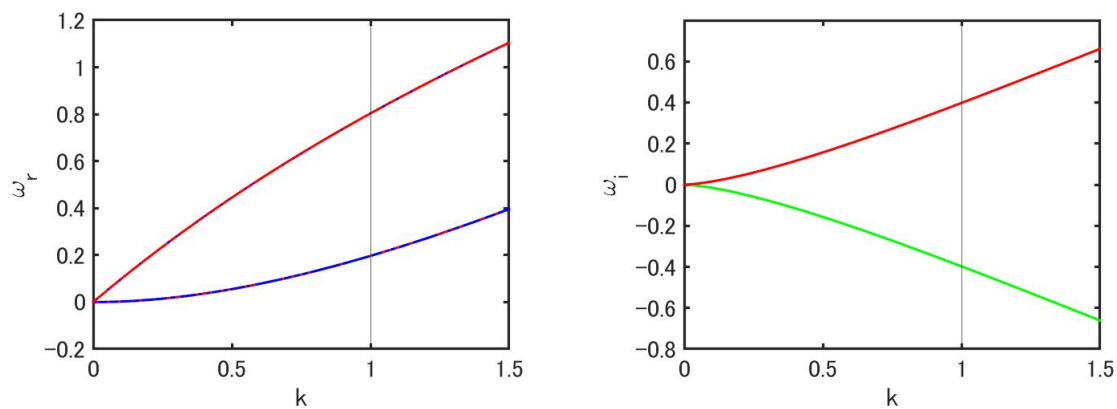

Figure 21. The (a) real and (b) imaginary parts of the dispersion curve in Case II given by (13) without density stratification ($\tilde{\rho}_0 = \tilde{\rho}_2 = 1$). The colors are the same as Figure 2, 3, and 4.
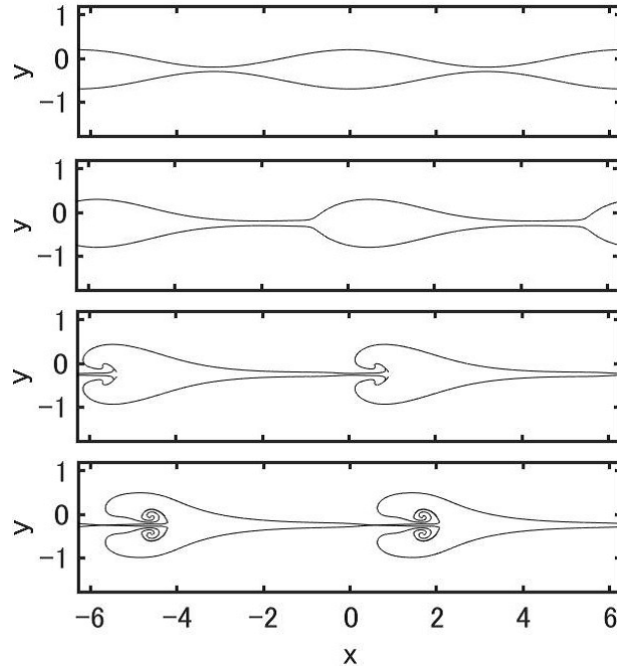
Figure 22. Interfacial structures without density stratification. The panels show $t = 0, \ 1, \ 2, \ 3$ from the top to the bottom.
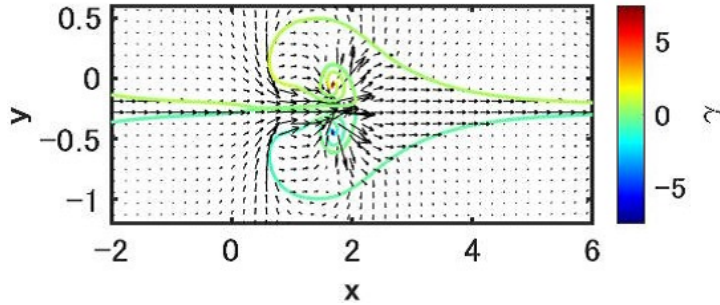

Figure 23. Velocity field without density stratification, where $t = 3$.

occurs at earlier times; however, the varicose structure itself is unchanged. As $\delta \to 0$, the curvature singularity [47] appears in the neighborhood of the narrowest part of the throat, and the calculation breaks down before the roll-up of interfaces occurs. Generally, too small values of δ ($\delta \le 0.05$) do not describe well the real vortex dynamics [30, 49].

Appendix B. Varicose structure without density stratification

For comparison, we provide the dispersion relation and the interfacial evolution for equidensity case in this appendix. We present the dispersion relation for Case II with $\tilde{\rho}_0 = \tilde{\rho}_2 = 1$ in Figure 21. The colors are the same as Figures 2, 3, and 4 in Section 2. In Figure 21 (a), the relations $\omega_1 = \omega_2$ (the black line coincides with the blue one) and

$\omega_3 = \omega_4$ (the green line coincides with the red one) hold, while the relations $\omega_1 = \omega_3$ (the black line coincides with the green one) and $\omega_2 = \omega_4$ (the blue line coincides with the red one) hold in Figure 21 (b). The closed region found in the range of $0 < k < 0.365$ in Figure 3 (a) disappears in Figure 21 (a), and the mutivaluedness in the corresponding range of k in Figure 3 (b) also disappears in Figure 21 (b). For this equidensity case, the detailed linear analysis is found in the reference [23].

Figure 23 shows the temporal evolution of the interfaces for the equidensity case ($\tilde{\rho}_0 = \tilde{\rho}_2 = 1$). The parameters except the density are the same as those for Case II in Section 4.3. The calculations are performed with $N = 2048$, $\triangle t = 6.25 \times 10^{-4}$, and $\delta = 0.1$. In the absence of the density stratification, the roll-up is symmetric. The velocity field at $t = 3$ (the lowest panel in Figure 22) is provided in Figure 23. A similar rectangular jet as Figure 17 is found in this figure as well.

[1] M. H. Aliabadi and P. Wen. *Boundary Element Methods In Engineering And Sciences.* World Scientific, 2011.

[2] P. Andersson, L. Brandt, A. Bottaro, and D. S. Henningson.

[3] G. R. Baker and J. Beale. Vortex blob methods applied to interfacial motion. *J. Compt. Phys.*, 196:233–258, 2003.

[4] G. R. Baker, R. Caflisch, and M. Siegel. Singularity formation during rayleigh-taylor instability. *J. Fluid Mech.*, 252:51–78, 1993.

[5] G. R. Baker, R. L. Mccrory, and C. P. Verdon. Rayleigh-taylor instability of fluid layers. *J. Fluid. Mech.*, 178:161–175, 1987.

[6] G. R. Baker, D. I. Meiron, and S. A. Orszag. Generalized vortex methods for free surface flow problems. *J. Fluid Mech.*, 123:477–501, 1982.

[7] G. R. Baker and L. Pham. A comparison of blob methods for vortex sheet roll-up. *J. Fluid Mech.*, 547:297–316, 2006.

[8] G. R. Baker and M. J. Shelley. On the connection between thin vortex layers and vortex sheets. *J. Fluid. Mech.*, 215:161–194, 1990.

[9] G. Birkhoff. Helmholtz and taylor instability. *Proc. Symp. Appl. Maths. Soc.*, 13:55–76, 1962.

[10] C. Börgers. On the numerical solution of the regularized birkhoff equations. *Math. Comput.*, 187:141–156, 1989.

[11] J. B. Bostwick and P. H. Steen. Static rivulet instabilities: varicose and sinuous modes. *J. Fluid Mech.*, 837:819–838, 2018.

[12] L. Brandt, C. Cossu, J-M. Chomaz, P. Huerre, and D. Henningson. On the convectively unstable nature of optimal streaks in boundary layers. *J. Fluid Mech.*, 485:221–242, 2003.

[13] M. A. Bucci, D. K. Puckert, C. Andriano, J.-Ch. Loiseau, S. Cherubini, J.-Ch. Robinet, and U. Rist. Roughness-induced transition by quasi-resonance of a varicose global mode. *J. Fluid Mech.*, 836:167–191, 2018.

[14] R. E. Caflisch and J. S. Lowengrub. Convergence of the vortex method for vortex sheets. *SIAM J. Numer. Anal.*, 26:1060–1080, 1989.

[15] M. J. Chen and L. K. Forbes. Steady periodic waves in a three-layer fluid with shear in the middle layer. *J. Fluid Mech.*, 594:157–181, 2008.

[16] A.J. Chorin and P.S. Bernard. Discretization of a vortex sheet with an example of roll-up. *J. Comput. Phys.*, 13:423–429, 1973.

[17] P. Colella and P. R. Woodward. The piecewise parabolic method (ppm) for gas-dynamical simulations. *J. Comput. Phys.*, 54:174–201, 1984.

[18] G-H. Cottet and P. D. Koumoutsakos. *Vortex methods: theory and practice.* Cambridge University Press, Cambridge, 2000.

[19] A. D. D. Craik. *Wave Interactions and Fluid Flows (Cambridge Monographs on Mechanics).* Cambridge University Press, Cambridge, 1988.

[20] A. D. D. Craik and J. A. Adam. Explosive' resonant wave interactions in a three-layer fluid flow. *J. Fluid Mech.*, 92:15–33, 1979.

[21] B. Cushman-Roisin and J.-M. Beckers. *Introduction to Geophysical Fluid Dynamics: Physical and Numerical Aspects.* Elsevier, Amsterdam, 2011.

[22] Si-C. Deng, C. Pan, and J-J. Wang. Dynamics of low-speed streak evolution and interaction in laminar boundary layer. *Acta Mech. Sinica*, 30:636–645, 2014.

[23] P. G. Drazin and L. N. Howard. *Hydrodynamic stability of parallel flow of inviscid fluid. In Advances in applied mechanics, vol. 7, ed. G. Kuerti.* Academic Press, New York, 1966.

[24] P. G. Drazin and W. H. Reid. *Hydrodynamic stability, 2nd ed.* Cambridge University Press, Cambridge, 2010.

[25] T. Y. Hou, J. S. Lowengrub, and R. Krasny. Convergence of a point vortex method for vortex sheets. *SIAM J. Numer. Anal.*, 28:308–320, 1991.

[26] T. Y. Hou, J. S. Lowengrub, and M. J. Shelley. Removing the stiffness from interfacial flows with surface tension. *J. Comput. Phys.*, 114:312–338, 1994.

[27] S. A. Jazayeri and X. Li. Nonlinear instability of plane liquid sheets. *J. Fluid Mech.*, 406:281–308, 2000.

[28] G. Kawahara, J. Jiménez, M. Uhlmann, and A. Pinelli. Linear instability of a corrugated vortex sheet - a model for streak instability. *J. Fluid Mech.*, 483:315–342, 2003.

[29] R. Krasny. A study of singularity formation in a vortex sheet by the point vortex approximation. *J. Fluid Mech.*, 167:65–93, 1986.

[30] R. Krasny. Computation of vortex sheet roll-up in the trefftz plane. *J. Fluid Mech.*, 184:123–155, 1987.

[31] H. G. Lee and J. Kim. Two-dimensional kelvin-helmholtz instabilities of multi-component fluids. *Euro. J. Mech. B/Fluids*, 49:77–88, 2015.

[32] L.-J. Liu, L.-J. Yang, and H.-Y. Ye. Weakly nonlinear varicose-mode instability of planar liquid sheets. *Phys. fluids*, 28:034105, 2016.

[33] W. Liu, X. Li, C. Yu, Y. Fu, P. Wang, L. Wang, and W. Ye. Theoretical study on finite-thickness effect on harmonics in richtmyer-meshkov instability for arbitrary atwood numbers. *Phys. Plasmas*, 25:122103, 2018.

[34] C. Matsuoka. Vortex sheet motion in incompressible richtmyer-meshkov and rayleigh-taylor instabilities with surface tension. *Phys. Fluids*, 21:092107, 2009.

[35] C. Matsuoka. Nonlinear dynamics of double-layer unstable interfaces with non-uniform velocity shear. *Phys. Fluids*, 32:102109, 2020.

[36] C. Matsuoka and K. Nishihara. Analytical and numerical study on a vortex sheet in incompressible richtmyer-meshkov instability in cylindrical geometry. *Phys. Rev. E*, 74:066303, 2006.

[37] C. Matsuoka and K. Nishihara. Fully nonlinear evolution of a cylindrical vortex sheet in incompressible richtmyer-meshkov instability. *Phys. Rev. E*, 73:055304(R), 2006.

[38] C. Matsuoka and K. Nishihara. Vortex core dynamics and singularity formations in incompressible richtmyer-meshkov instability. *Phys. Rev. E*, 73:026304, 049902(E), 2006.

[39] C. Matsuoka and K. Nishihara. Nonlinear interaction between bulk point vortices and an unstable interface with nonuniform velocity shear such as richtmyer-meshkov instability. *Phys. Plasmas*, 27:052305, 2020.

[40] C. Matsuoka, K. Nishihara, and F. Cobos-Campos. Linear and nonlinear interactions between an interface and bulk vortices in richtmyer-meshkov instability. *Phys. Plasmas*, 27:052305, 2020.

[41] C. Matsuoka, K. Nishihara, and T. Sano. Nonlinear dynamics of non-uniform current-vortex sheets in magnetohydrodynamic flows. *J. Nonlinear Sci.*, 27:531–572, 2017.

[42] E. E. Meshkov. Instability of the interface of two gases accelerated by a shock wave. *Sov. Fluid Dynamics*, 4:101–108, 1969.

[43] K. O. Mikaelian. Normal modes and symmetries of the rayleigh-taylor instability in stratified fluids. *Phys. Rev. Lett.*, 19:1365–1368, 1982.

[44] K. O. Mikaelian. Rayleigh-taylor instabilities in stratified fluids. *Phys. Rev. A*, 26:2140–2158, 1982.

[45] K. O. Mikaelian. Time evolution of density perturbation in accelerating stratified fluids. *Phys. Rev. A*, 28:1637–1646, 1983.

[46] K. O. Mikaelian. Richtmyer-meshkov instabilities in stratified fluids. *Phys. Rev. A*, 31:410–419, 1985.

[47] D. W. Moore. The spontaneous appearance of a singularity in the shape of an evolving vortex sheet. *Proc. Roy. Soc. A*, 365:105–119, 1979.

[48] K. Nishihara, J. G. Wouchuk, C. Matsuoka, R. Ishizaki, and V. V. Zhakhovskii. Richtmyer-meshkov instability: theory of linear and nonlinear evolution. *Phil.Trans. Roy. Soc. A*, 368:1769–1807, 2010.

[49] M. Nitsche and R. Krasny. A numerical study of vortex ring formation at the edge of a circular tube. *J. Fluid Mech.*, 276:139–161, 1994.

[50] S. Panda, S. C. Martha, and A. Chakrabarti. Three-layer fluid flow over a small obstruction on the bottom of a channel. *Anziam J.*, 56:248–274, 2015.

[51] S. Ravier, M. Abid, M. Amielh, and F. Anselmet. Direct numerical simulations of variable-density plane jets. *J. Fluid Mech.*, 546:153–191, 2006.

[52] R. D. Richtmyer. Taylor instability in shock acceleration of compressible fluids. *Commun. Pure Appl. Math.*, 13:297–319, 1960.

[53] N. Rott. Diffraction of a weak shock with vortex generation. *J. Fluid Mech.*, 1:111–128, 1956.

[54] P. G. Saffman. *Vortex Dynamics*. Cambridge University Press, Cambridge, 1992.

[55] T. Sano, T. Inoue, and K. Nishihara. Critical magnetic field strength for suppression of the richtmyer-meshkov instability in plasmas. *Phys. Rev. Lett.*, 111:205001, 2013.

[56] T. Sano, K. Nishihara, C. Matsuoka, and T. Inoue. Magnetic field amplification associated with the richtmyer-meshkov instability. *Astrophys. J.*, 758:126, 2012.

[57] M. J. Shelley. A study of singularity formation in vortex-sheet motion by a spectrally accurate vortex method. *J. Fluid Mech.*, 244:493–526, 1992.

[58] A. Sidi and M. Israeli. Quadrature methods for periodic singular and weakly singular fredholm integral equations. *J. Sci. Compt.*, 3:201–231, 1998.

[59] M. Skote, J. H. Haritonidis, and D. S. Henningson. Varicose instabilities in turbulent boundary layers. *Phys. Fluids*, 14:2309–2323, 2002.

[60] W. D. Smyth and J. R. Carpenter. *Instability in Geophysical flows*. Cambridge University Press, Cambridge, 2019.

[61] B. R. Sutherland. *Internal gravity waves*. Cambridge University Press, Cambridge, 2010.

[62] N. Zabusky. Vortex paradigm for accelerated inhomogeneous flows: visiometrics for the rayleigh-taylor and richtmyer-meshkov environments. *Annu. Rev. Fluid Mech.*, 31:495–536, 1999.

[63] N. J. Zabusky and S. Zhang. Shock-planar curtain interactions in two dimensions: Emergence of vortex double layers, vortex projectiles, and decaying stratified turbulence. *Phys. Fluids*, 14:419–422, 2002.